Geophysical Journal International Advance Access published September 28, 2013

Joint microseismic location and anisotropic tomography using differential arrival times and differential backazimuths

Junlun Li,[1] Haijiang Zhang,[1,2] William L. Rodi[1] and M. Nafi Toksoz[1]

[1]*Earth Resources Laboratory, Department of Earth, Atmospheric and Planetary Sciences, Massachusetts Institute of Technology,* 77 *Massachusetts Avenue, Cambridge, MA* 02139, *USA. E-mail: junlunli@mit.edu*

[2]*Laboratory of Seismology and Physics of Earth's Interior, University of Science and Technology of China, Hefei, Anhui Province* 230026, *China*

SUMMARY

We develop a new method to locate microseismic events induced by hydraulic fracturing with simultaneous anisotropic tomography, using differential arrival times and differential backazimuths. Compared to the existing double-difference method, our method incorporates backazimuth information to better constrain microseismic locations in the case of downhole linear seismic arrays used for monitoring induced seismicity. The tomography is constrained to a 1-D layered VTI (transversely isotropic structure with a vertical symmetry axis) structure to improve inversion stability given the limited passive seismic data. We derive analytical sensitivities for the elastic moduli (C_{ij}) and layer thickness L, and verify the analytical results with numerical calculations. The forward modelled traveltimes and sensitivities are all calculated analytically without weak anisotropy assumption. By incorporating the relative information among events, the extended double-difference method can provide better relative locations for events and, therefore, can characterize the fractures with higher accuracy. In the two tests with synthetic data, our method provides more accurate relative locations than the traditional methods, which only use absolute information. With fast speed and high accuracy, our inversion scheme is suitable for real-time microseismic monitoring of hydraulic fracturing.

Key words: Downhole methods; Fracture and flow; Body waves; Seismic anisotropy; Seismic tomography; Seismic anisotropy.

GJI Seismology

1 INTRODUCTION

Microseismic monitoring is a commonly used and promising technique for characterizing the development of hydraulic fracturing in shale gas/oil play (Rutledge & Phillips 2003; Maxwell *et al.* 2010; Zimmer 2011; Li *et al.* 2011). However, there are several hindrances to the practical use of this technique: (1) the fracturing induced seismic events are generally weak and difficult to detect; (2) for the detected events, accurate picking of the first *P*- and *S*-wave arrival times and reliably determining their arriving backazimuths are sometimes difficult due to noise contamination; (3) even with good readings, the location of microseismic events is still prone to error due to the lack of an accurate velocity model, for example, in gas/oil shale cases where strong VTI anisotropy (up to 30 per cent) is commonly seen (Warpinski *et al.* 2009). Fig. 1 shows some significant delay of the SV wave compared to the SH wave from a microseismic event due to anisotropy in shale during a hydraulic fracturing job. Perforation shots are often used to calibrate the velocity model for locating the microseismicity induced during the injection stages (Warpinski *et al.* 2005; van Dok *et al.* 2011). However, anisotropy and heterogeneity in the velocity structure can result in location errors if the induced events do

not collocate with the perforation shots because the wave propagation paths differ. In many hydraulic fracturing treatments, fracturing often does not occur in the vicinity of the perforation shots and can be a few hundred metres away (e.g. Rutledge *et al.* 1998; Rutledge & Phillips 2003). Therefore it is problematic to locate the microseismicity if only the velocity model constructed from the perforation shots is used. Furthermore, when events are located individually, the variability in location error among the events makes it difficult to delineate fractures (Eisner *et al.* 2010; Maxwell 2010; Grechka *et al.* 2011).

For tackling the first issue, Song *et al.* (2010) used the waveform similarity for neighboring induced microseismic events to detect weaker events by forming a library of waveform templates from stronger events. In this study, we aim to deal with the second and third issues. Taking advantage of the waveform similarity, we can obtain more accurate differential arrival times for nearby microseismic events. Using the more accurate differential times, relative seismic locations can be better determined with the double-difference location method. It has the ability to remove common errors in both model and data that exist among closely spaced microseismic events (Waldhauser & Ellsworth 2000; Wolfe 2002; Zhang & Thurber 2003).
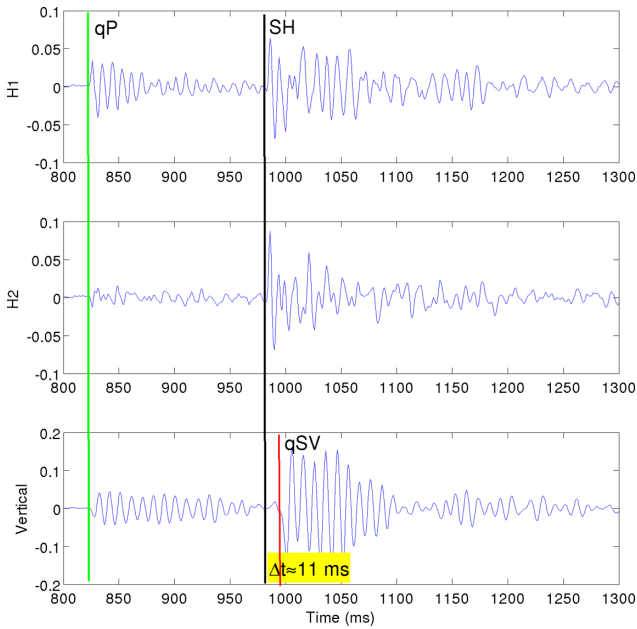
Figure 1. Recorded three-component seismograms from a microseismic event induced by shale-gas hydraulic fracturing. qP, SH and qSV phase arrivals are marked by green, black and red lines. It clearly shows the SH wave arrives about 11 ms earlier than the qSV wave, indicating strong anisotropy in shale.

For microseismic monitoring, however, in many cases linear seismic arrays deployed in boreholes are used. To better constrain microseismic locations, backazimuth information of seismic waves arriving at different sensors is needed. The backazimuths can be determined either from *P* waves or from SH waves in a layered medium with VTI anisotropy. The SH waves usually have larger amplitudes but are also contaminated by *P*-wave coda. De Meersman *et al.* (2009) improved the locations of induced microseismicity in North Sea Valhall oil field with simultaneously estimated backazimuths for all stations within an array using a noise-weighted Singular Value Decomposition (SVD) of the complex analytic signals, together with better traveltime picks. Rutledge & Phillips (2003) determined the induced event locations in Cotton Valley with both traveltime and backazimuth information. They improved relative event locations by extracting more consistent arrival time picks from peaks and troughs of similar time-interpolated waveforms. It should be noted that small-unaccounted deviation of the borehole could result in considerable errors in determining the azimuthal distribution of the fractures (Bulant *et al.* 2007). In our paper, we extend the double-difference method to include backazimuths from *P* waves in addition to arrival times. Similar to differential arrival times, we expect that differential backazimuths are also more accurate than the absolute values due to common errors. As a result, the new double-difference method using both differential times and backazimuths is able to better determine relative seismic locations.

When the event locations and origin times are known, anisotropic tomography can be greatly simplified. In ideal cases such as experiments, if compressional and shear waves that propagate horizontally and vertically in a homogeneous space are recorded with waves propagating in other directions, then the parameters of a VTI medium can be determined separately and the tomography for a homogeneous space can be greatly simplified (Nihei *et al.* 2011). In real cases, however, it is very uncommon to have such an ideal

source–receiver geometry. Mah & Schmitt (2003) used a global search method to simultaneously determine all elastic moduli of a homogenous composite material from traveltimes. However, the computer time required by their method increases very rapidly with the number of observations and unknown parameters. To obtain a velocity model that better reflects the structure between the actual microseismicity and the receivers, Grechka *et al.* (2011) simultaneously estimated the general anisotropy of the medium while locating the microseismicity, assuming the medium is a homogeneous anisotropic space. However, the receiver array often spans a large depth range and is likely to be in a very different formation from where the microseismic events are located. As a result, it could be unrealistic to assume the medium to be homogeneous in these cases. Zhang *et al.* (2009) estimated the heterogeneous isotropic velocity structure in an oil/gas reservoir with the double-difference tomography method of Zhang & Thurber (2003). This method simultaneously locates seismic events and determines the velocity model by using differential traveltimes and absolute picks from reservoir induced seismic events. However, their ideal azimuthal coverage with five monitoring wells is rarely seen in hydraulic fracturing cases, and the anisotropy in the reservoir was not addressed in their study. It should be noted that sometimes an artificial effect of anisotropy may appear in traveltimes observed in boreholes if the deviation of the borehole is not correctly taken into account (Bulant *et al.* 2007).

Considering the above problems, our study focuses on determining the anisotropic structure of the medium and locations of the microseismic events: (1) we develop a new anisotropy tomography method to determine the anisotropic structure between the microseismic events and the receiver array using arrival time picks (qP, qSV and SH), with the structure assumed to be a 1-D layered VTI medium given the limited spatial coverage of passive microseismic observations; (2) we extend the double-difference location method to use more accurate differential arrival times (Waldhauser & Ellsworth 2000; Zhang & Thurber 2006; Foulger & Julian 2011; Castellanos *et al.* 2012) and differential backazimuths to better constrain the relative event locations. The layer approximation of the velocity structure is considered to be reasonable in most downhole microseismic monitoring cases, especially in the hydraulic fracturing cases, where the medium mainly consists of flat sedimentary rocks (e.g. Rutledge *et al.* 1998; Warpinski *et al.* 2005), and the epicentral distance between events and sensors often varies from a few tens to a few hundreds of metres. The velocity tomography using absolute picks is important to determine the absolute locations of the events, while the differential observations are critical to improve the relative locations and better delineate the fractures (Zhang *et al* 2009).

In this study, we derive analytically sensitivities for the elastic moduli (C_{ij}) and layer thickness (*L*) in our seismic location and tomography algorithm without any weak anisotropy assumption. Utilizing a method for calculating the traveltimes of qP, qSV and SH waves analytically (Tang & Li 2008), our inversion scheme is fast and accurate, and especially suitable for real time monitoring.

2 METHODOLOGY

2.1 Microseismic location with differential arrival times and backazimuths

Let us denote the observed arrival time from event *i* to station *k* as $^{o}t_{k}^{i}$ and the corresponding modelled arrival time as $^{m}t_{k}^{i}$ from initial event location and velocity model. The conventional seismic

location method simply relates the arrival time residual to the perturbations in event location and origin time by assuming the velocity model is known:

$$^t r_k^i = {}^o t_k^i - {}^m t_k^i = \sum_{l=1}^{3} \frac{\partial T_k^i}{\partial x_l} \Delta x_l^i + \Delta \tau^i, \tag{1}$$

where x_l ($l = 1, 2, 3$) denotes seismic locations in three dimensions, T_k^i is the traveltime, and τ^i is the origin time. If we take the difference between the arrival time residuals from event pairs i and j to a common station k, it becomes the double-difference location method first proposed by Waldhauser & Ellsworth (2000) as follows:

$$^t r_k^i - {}^t r_k^j = \sum_{l=1}^{3} \frac{\partial T_k^i}{\partial x_l^i} \Delta x_l^i + \Delta \tau^i - \sum_{l=1}^{3} \frac{\partial T_k^j}{\partial x_l^j} \Delta x_l^j - \Delta \tau^j, \tag{2}$$

where the difference can also be defined as

$$^t r_k^i - {}^t r_k^j = \left(t_k^i - t_k^j \right)^o - \left(t_k^i - t_k^j \right)^m. \tag{3}$$

The double-difference method is capable of eliminating the unmodelled common errors existing along the ray paths between a closely spaced cluster of events and a receiver (Zhang & Thurber 2006). In an anisotropic model, the sensitivity of the traveltime with respect to the hypocentre is simply the phase slowness p_1 at the source location,

$$\frac{\partial T_k^i}{\partial x_l^i} = p_l^i \tag{4}$$

and the sensitivity of the traveltime with respect to the origin time is unity (eq. (1)). Note in isotropic media the phase slowness and group slowness are the same.

We extend the double-difference location method using differential arrival times (Waldhauser & Ellsworth 2000) to include *P*-wave arrival backazimuths. The notations for backazimuth in the following are similar to those for arrival time. First, the residual between the observed and modelled backazimuths can be expressed as

$$^\varphi r_k^i = \sum_{l=1}^{3} \frac{\partial \varphi_k^i}{\partial x_l^i} \Delta x_l^i \tag{5}$$

and the corresponding double-difference form is

$$^\phi r_k^i - {}^\varphi r_k^j = \sum_{l=1}^{3} \frac{\partial \varphi_k^i}{\partial x_l^i} \Delta x_l^i - \sum_{l=1}^{3} \frac{\partial \varphi_k^j}{\partial x_l^j} \Delta x_l^j, \tag{6}$$

where $^\varphi r$ is the backazimuth residual. In ray approximation, the backazimuth angle can be expressed as:

$$\tan \left(\varphi_k^i \right) = \frac{\partial T_k^i / \partial y_r}{\partial T_k^i / \partial x_r} \tag{7}$$

with horizontal slowness vector, where $\partial T_k^i / \partial x_r$ and $\partial T_k^i / \partial y_r$ are the traveltime derivatives with respect to x and y coordinates at the receiver location, respectively. We define the positive x-axis as the zero backazimuth angle, and the angle increases counter-clockwise. In a heterogeneous medium, the sensitivity of the backazimuth with respect to the hypocentre can be derived from eq. (7):

$$\frac{\partial \varphi_k^i}{\partial x_l} = \alpha_1 \frac{\partial \left(\frac{\partial T_k^i}{\partial y_r} \right)}{\partial x_l^i} + \alpha_2 \frac{\partial \left(\frac{\partial T_k^i}{\partial x_r} \right)}{\partial x_l^i}, \tag{8}$$

where

$$\alpha_1 = \frac{1}{\partial T_k^i / \partial x_r} \frac{1}{1 + \left(\frac{\partial T_k^i / \partial y_r}{\partial T_k^i / \partial x_r} \right)^2}$$

$$\alpha_2 = -\frac{1}{\left(\partial T_k^i / \partial x_r \right)^2} \frac{\partial T_k^i / \partial y_r}{1 + \left(\frac{\partial T_k^i / \partial y_r}{\partial T_k^i / \partial x_r} \right)^2}. \tag{9}$$

In Appendix A, we show how to approximate eq. (8) with the finite difference calculation. For a 1-D layered VTI velocity structure where the backazimuths can be directly given by the source–receiver geometries, the sensitivities with respect to the hypocentre can be expressed as:

$$\frac{\partial \varphi}{\partial x_s} = -\frac{y_s - y_r}{(x_s - x_r)^2 + (y_s - y_r)^2}$$

$$\frac{\partial \varphi}{\partial y_s} = \frac{x_s - x_r}{(x_s - x_r)^2 + (y_s - y_r)^2}$$

$$\frac{\partial \varphi}{\partial z_s} = 0. \tag{10}$$

The differential backazimuth angles can be calculated by differentiating two angles obtained from the eigenvectors of the covariance matrix of the seismograms (Magotra *et al.* 1989), or can be calculated independently with the method described in Appendix B.

To demonstrate how the extended double-difference method can reduce the common traveltime and backazimuth errors for closely spaced events, we create an anisotropic heterogeneous model by adding strong random perturbation to a VTI layer model (Fig. 2). For a VTI medium, the property of anisotropy can be characterized by five independent elastic moduli $C_{11}, C_{13}, C_{33}, C_{55}$ and C_{66}. Alternatively, the property can be characterized by the Thomsen's parameters (Thomsen 1986), which are the vertical *P*-wave velocity α_0, the vertical *S*-wave velocity β_0 and three anisotropy parameters ε, δ and γ. In the following discussions, we actually use the density-normalized elastic moduli $\widetilde{C}_{ij}$, (defined as $\widetilde{C}_{ij} = \frac{C_{ij}}{\rho}$), but for simplification we still use C_{ij} to represent $\widetilde{C}_{ij}$. The random perturbation is on the elastic moduli, and for a certain location the
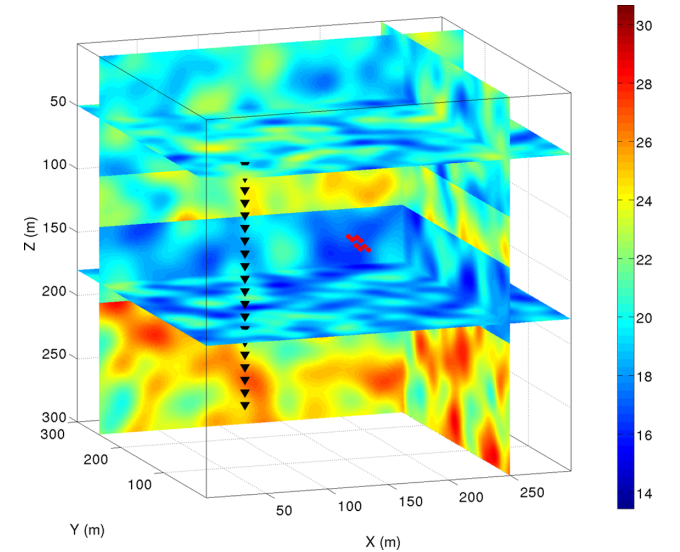

Figure 2. Randomly perturbed model for C_{11} (Gpa cm^3 g^{-1}). The model is constructed by adding spatially correlated ($L_c = 10$ m) random Gaussian noise to a VTI layer model. One fracture system with two parallel fractures is shown here. The epicentre distance from the centre of the fracture system to the receiver array is about 230 m. The parallel fractures trend in 45° in the *X*–*Y* plane, and the dipping angles (away from the vertical direction) are about 55°.

perturbations on the five elastic moduli (C_{11}, C_{13}, C_{33}, C_{55}, C_{66}) are the same in percentage, for example, the anisotropic parameters ε, δ and γ are invariant after the perturbation, while the vertical velocity α_0 and β_0 are perturbed randomly (*cf.* eq. (8), Thomsen 1986). The random Gaussian heterogeneity $\delta C(x, y, z)$ has correlation length about 10 m and peak amplitude about 0.15. The perturbation can be expressed as:

$$C_{ij}(x, y, z) = C_{ij}^0(x, y, z) + \delta C(x, y, z) \cdot C_{ij}^0(x, y, z). \qquad (11)$$

In this model, we create eight closely spaced events in two neighboring parallel fractures (four events on each fracture). We used an in-house finite-difference wave propagation code (fourth order in space, second order in time) to generate synthetic seismograms (Moczo *et al.* 2007), and we manually picked the arrival times for qP, qSV and SH in each seismogram at their first breaks. The events within a cluster are ordered (1–4) starting from the closer end to the receiver array to the distant end in one fracture, and then similarly for the other parallel fracture (5–8).

Fig. 3 shows the traveltimes and backazimuths determined from the synthetic seismograms. For the traveltimes, a similar trend of variation can be found for all events, indicating a similar propagation path while occasional abrupt changes among the picks at a common receiver are due to picking errors and influences from small heterogeneities that only affect some events. The determined backazimuths from the waveforms are heavily biased by the heterogeneity, and vary in a quite wide range ($\sim$39° to $\sim$55°), compared to a much smaller theoretical range ($\sim$47.5° to $\sim$49.5°, shaded box) in a case without random heterogeneity. The heterogeneities in this model have larger influence on the backazimuths in comparison with the influence on the traveltimes, which are mostly perturbed by less than a few percent (not plotted for clarity). However, at a certain receiver the variation of the backazimuths among different events is small, for example, usually less than a few degrees. This synthetic data indicates when the differential backazimuth information is included in the inversion, the events should be located more accurately in a tighter azimuthal range.
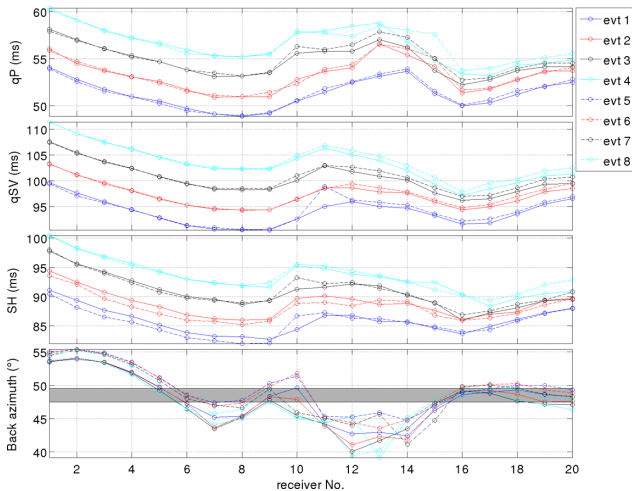

Figure 3. Traveltimes for qP, qSV, SH phases and backazimuths from eight events in a cluster. The shaded box indicates the theoretical backazimuths that would be observed if the medium is a VTI layer structure without random perturbations.

2.2 Strong anisotropic tomography for 1-D layered VTI structure

In our study, we parametrize the velocity structure as 1-D layers with different elastic modulus C_{ij} ($ij = 11, 13, 33, 55, 66$) and thickness L for each layer. First, we study the sensitivity with respect to elastic modulus. For a VTI medium, the phase velocity v for qP, qSV and SH waves with phase angle θ are given by (e.g. Thomsen 1986; Tang & Li 2008):

$$\rho v_p^2(\theta) = \frac{1}{2}[C_{33} + C_{55} + (C_{11} - C_{33})\sin^2(\theta) + D(\theta)]$$

$$\rho v_{SV}^2(\theta) = \frac{1}{2}\left[C_{33} + C_{55} + (C_{11} - C_{33})\sin^2(\theta) - D(\theta)\right]$$

$$\rho v_{SH}^2(\theta) = C_{66}\sin^2(\theta) + C_{55}\cos^2(\theta), \qquad (12)$$

where

$$D(\theta) = \Big\{(C_{33} - C_{55})^2 + 2\big[2(C_{13} + C_{55})^2 - (C_{33} - C_{55}) \\ \times (C_{11} + C_{33} - 2C_{55})\big]\sin^2(\theta) + \big[(C_{11} + C_{33} - 2C_{55})^2 \\ - 4(C_{13} + C_{55})^2\big]\sin^4(\theta)\Big\}^{\frac{1}{2}}. \qquad (13)$$

2.2.1 Sensitivity with respect to elastic moduli

The sensitivity of traveltime T with respect to the elastic modulus C_{ij} in layer k is:

$$\frac{\partial T^k}{\partial C_{ij}^k} = \frac{\partial\left(\frac{l^k}{v_g^k}\right)}{\partial C_{ij}^k} = -\frac{l^k}{\left(v_g^k\right)^2}\frac{\partial v_g^k}{\partial C_{ij}^k}, \qquad (14)$$

where l^k is the ray path within layer k and v_g^k is the group velocity in layer k. Note the derivative depends on the group velocity, thus the anisotropic tomography problem becomes nonlinear. Using the relation between the phase and group velocities (Thomsen 1986; Tang & Li 2008), the sensitivity of the group velocity with respect to the elastic modulus is:

$$\frac{\partial v_g}{dC_{ij}} = \frac{1}{2v_g}\frac{\partial v_g^2}{dC_{ij}} = \frac{1}{2v_g}\frac{\partial\left(v^2 + \frac{1}{4v^2}\left(\frac{\partial v^2}{\partial \theta}\right)^2\right)}{\partial C_{ij}}$$

$$= \frac{1}{2v_g}\left[\frac{\partial v^2}{\partial C_{ij}}\left(1 - \frac{1}{4v^4}\left(\frac{\partial v^2}{\partial \theta}\right)^2\right) + \frac{1}{2v^2}\frac{\partial v^2}{\partial \theta}\frac{\partial\left(\frac{\partial v^2}{\partial \theta}\right)}{\partial C_{ij}}\right]. \qquad (15)$$

Eq. (15) is a general expression for qP, qSV and SH. However, the terms $\partial v^2/\partial C_{ij}$ and $\partial(\frac{\partial v^2}{\partial \theta})/\partial C_{ij}$ change for different types of waves. The derivation of these derivatives for qP, qSV and SH is given in Appendix C. We noticed Zhou & Greenhalgh (2005) derived analytical expressions of the sensitivities with respect to elastic moduli in VTI medium in different forms and with a quite different approach.

2.2.2 Sensitivity with respect to layer thickness

Here we study the sensitivity with respect to the layer thickness L. The perturbation of the ray path and traveltime caused by the change of the layer thickness (or interface position) is illustrated in Fig. 4.
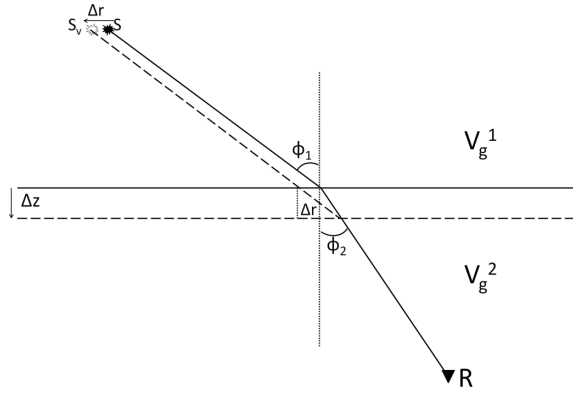
Figure 4. Ray path and traveltime perturbations caused by layer interface change. S denotes the source and R denotes the receiver. The group angle and group velocity are Φ_1, V_g^1 in the first medium, and Φ_2, V_g^2 in the second medium, respectively. The original ray is denoted by the solid line and the perturbed interface and ray are denoted by the dashed lines.

Obeying Snell's law, we consider a virtual source S_v emits a parallel ray (dashed) that hits the perturbed interface and is converted to the same ray (solid) in the second medium. Here we decompose the traveltime perturbation into two parts: (1) the perturbation caused by changing the original source S to the virtual source S_v; (2) the perturbation within Δz caused by group velocity change (V_g^1 to V_g^2) and ray path change (solid to dashed). It should be emphasized that when the interface location is perturbed, the actual ray will change its paths in both layers and, in fact, does not coincide with either the solid or the dashed rays shown in Fig. 4. The sensitivity decomposition above is just an exact alternative expression for the traveltime perturbation. For the first part of the sensitivity, that is, the traveltime perturbation due to the source location changing from S to S_v as the result of the interface perturbation Δz, the sensitivity is

$$S_1 = \frac{\partial T}{\partial z} = \frac{\partial T}{\partial r}\frac{\partial r}{\partial z} = \frac{\partial T}{\partial r}\frac{-[\Delta z \tan(\Phi_1) - \Delta z \tan(\Phi_2)]}{\Delta z}$$

$$= \frac{\partial T}{\partial r}[\tan(\Phi_2) - \tan(\Phi_1)], \qquad (16)$$

where the negative sign appears due to the coordinate definition (moving to the negative X-axis). $\partial T/\partial r$ is the horizontal (radial) phase slowness p_r.

For the sensitivity in the perturbation region Δz, we have

$$S_2 = \frac{\frac{L_{dash}}{V_g^1} - \frac{L_{solid}}{V_g^2}}{\Delta z} = \frac{\frac{\Delta z}{\cos(\Phi_1)V_g^1} - \frac{\Delta z}{\cos(\Phi_2)V_g^2}}{\Delta z}$$

$$= \frac{1}{\cos(\Phi_1)V_g^1} - \frac{1}{\cos(\Phi_2)V_g^2}. \qquad (17)$$

Then finally we can express the sensitivity of the traveltime with respect to the layer thickness, or the interface position as

$$\frac{\partial T}{\partial L} = S_1 + S_2 = p_r[\tan(\Phi_2) - \tan(\Phi_1)] + \frac{1}{\cos(\Phi_1)V_g^1}$$

$$- \frac{1}{\cos(\Phi_2)V_g^2}. \qquad (18)$$

Here we derived the exact sensitivity without the need to recalculate the ray path. It should be noted that although our derivation is based on a simple two-layer model, the sensitivity expression $\partial T/\partial L$ is actually valid for any multilayer case. For any intermediate layers between the source and the receiver in a multilayer case, the source and receiver positions shown above are simply replaced

by the intersection point of the rays with the layer interfaces. The sensitivity expression remains the same for each layer. Although we derived the sensitivity in a situation where the top layer has a faster wave speed than the bottom layer, the sensitivity expression remains the same if the top layer has a slower wave speed. If the ray travels upwards, a negative sign should be added to the sensitivity $\partial T/\partial L$.

2.3 Scheme for hypocentre location with simultaneous anisotropic tomography

The inversion scheme for determining both the velocity structure and the hypocentres can be written in the following form:

$$\begin{bmatrix} \boldsymbol{Q}_{DD}^t \boldsymbol{A}^t \\ \boldsymbol{Q}_{DD}^\varphi \boldsymbol{A}^\varphi \\ w^t \boldsymbol{A}^t \\ w^\varphi \boldsymbol{A}^\varphi \\ w^c \boldsymbol{P}^c \end{bmatrix} \begin{bmatrix} \Delta \boldsymbol{C}_{ij} \\ \Delta \boldsymbol{L} \\ \Delta \boldsymbol{X} \end{bmatrix} = \begin{bmatrix} \boldsymbol{Q}_{DD}^t \Delta \boldsymbol{T} \\ \boldsymbol{Q}_{DD}^\varphi \Delta \boldsymbol{\varphi} \\ w^t \Delta \boldsymbol{T} \\ w^\varphi \Delta \boldsymbol{\varphi} \\ -w^c \boldsymbol{P}^c \boldsymbol{C}_{ij}^0 \end{bmatrix}, \qquad (19)$$

where $\boldsymbol{Q}_{DD}^t$ and $\boldsymbol{Q}_{DD}^\varphi$ are the differential matrices for traveltimes (Wolfe 2002; Zhang & Thurber 2006) and backazimuths, respectively, and $\boldsymbol{Q}_{DD}^\varphi$ is constructed similarly to $\boldsymbol{Q}_{DD}^t$; w^t and w^φ are the relative weights for absolute traveltimes and backazimuths, respectively; $\boldsymbol{A}^t = [\boldsymbol{M}^t \boldsymbol{H}^t]$ is the sensitivity matrix of the traveltime with respect to the velocity structure ($\boldsymbol{M}^t$, eqs 14 and 18), and the event hypocentres ($\boldsymbol{H}^t$, eq. 4); $\boldsymbol{A}^\varphi = [0 \ \boldsymbol{H}^\varphi]$ is the sensitivity matrix of the backazimuth with respect to the hypocentres (eq. 10); $\boldsymbol{P}^c$ is the constraint operator on $\boldsymbol{C}_{ij}$ that attempts to retain some well-determined anisotropic parameters ε, δ or γ from core sample measurements in the lab (Chang Li, personal communication; Appendix D). $\Delta \boldsymbol{C}_{ij}$ is the perturbation on the elastic moduli, and $\Delta \boldsymbol{L}$ is the perturbation on the layer thickness; $\Delta \boldsymbol{X}$ is the perturbation on hypocentre and origin time of events; $\Delta \boldsymbol{T}$ is the traveltime residual, and $\Delta \boldsymbol{\varphi}$ is the backazimuth residual. Note since we assume 1-D layered VTI structure, the sensitivity of the backazimuth with respect to the velocity structure is null.

In our inversion, we parametrize the density normalized elastic moduli with the unit of Gpa cm^3 g^{-1}, as we found such parametrization would make the sensitivity more balanced for elastic moduli, layer thicknesses (metre) and source parameters (metre for hypocentre, second for origin time). The Levenberg–Marquardt algorithm (Levenberg 1944) is used for the inversion. We iterate the inversion until the reduction in residuals becomes negligible. Also, as local minima exist in this nonlinear inverse problem, different damping parameters were tried in the inversion to obtain the best results.

3 NUMERICAL EXAMPLES AND DISCUSSIONS

In this section, we show two examples of joint microseismic location and anisotropic tomography using differential data. In the first example, a model with strong anisotropic layers is used for the test (Fig. 5). The model has four layers and three interfaces. There are two fracture systems in the model with two neighboring parallel fractures in each system and each fracture is associated with four events. The general trend of the fracture system is similar to that shown in Fig. 2. In total there are 16 events used as passive sources for the anisotropic tomography. The traveltime data for this example are generated with the analytic ray shooting method by Tang & Li
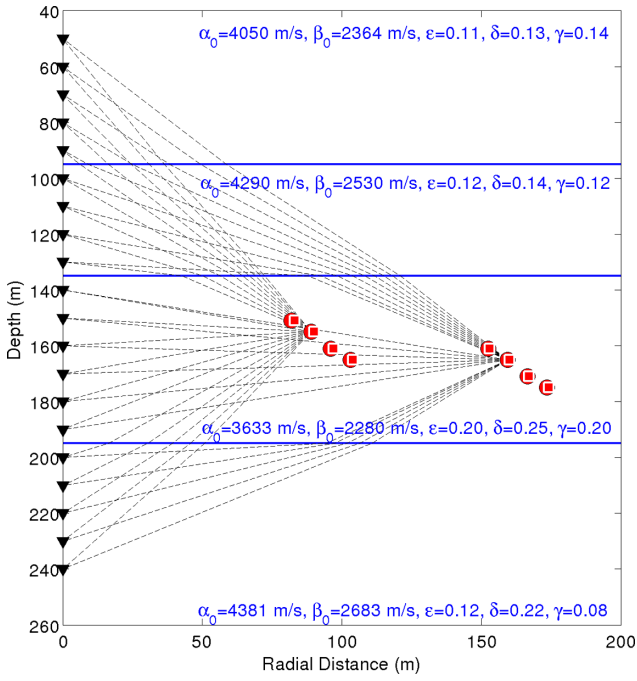
Figure 5. 1-D layered anisotropic model with receivers (black triangles) and events (red dots and red squares with white edges). Note: this is a side view of a 3-D model with each event projected onto its radial plane to clearly show the ray angles. The backazimuths of the events differ. The layers from top to bottom are numbered 1–4, respectively. The qP ray paths from selected events are illustrated with the dashed lines to show the ray angle coverage. In this synthetic model, there are 20 receivers numbered 1–20 from top to bottom. There are two fracture systems separated at about 50 m in the horizontal direction. In each fracture system, there are two fractures with four events associated with each fracture.

(2008), and the backazimuth data are determined from the source–receiver geometry. Note, Fig. 5 shows the projections of events and ray paths in the radial planes for clarity, and the backazimuths of the events are different. We assume randomly half of the receivers have readings of the qP, qSV, SH and backazimuth θ for each event to resemble a realistic noisy situation or variation in array sensitivity. The random receiver choice is different for different traveltime phases as well as for backazimuths. The qP ray paths from one event in each cluster are illustrated with the dashed lines to show the ray angle coverage. The qSV and SH ray paths deviate from the qP ray paths due to different contrast between layers. However, the deviations are minor in this case and thus are not shown for avoiding redundancy.

We first examine the analytical derivation of the sensitivity with respect to the elastic modulus and layer thickness. We can use numerical second-order central differencing to approximate the derivative:

$$\frac{\partial T}{\partial C_{ij}} \approx \frac{T\left(C_{ij} + \Delta C\right) - T\left(C_{ij} - \Delta C\right)}{2\Delta C} \tag{20}$$

and

$$\frac{\partial T}{\partial L_k} \approx \frac{T\left(L_K + \Delta L\right) - T\left(L_k - \Delta L\right)}{2\Delta L}. \tag{21}$$

For each perturbed parameter the traveltime is computed accurately with an analytical method (Tang & Li 2008). Therefore, the numerical difference can achieve great accuracy by using a very small increment. The numerical derivatives, though time-consuming to calculate, can be used as the reference. Note in the
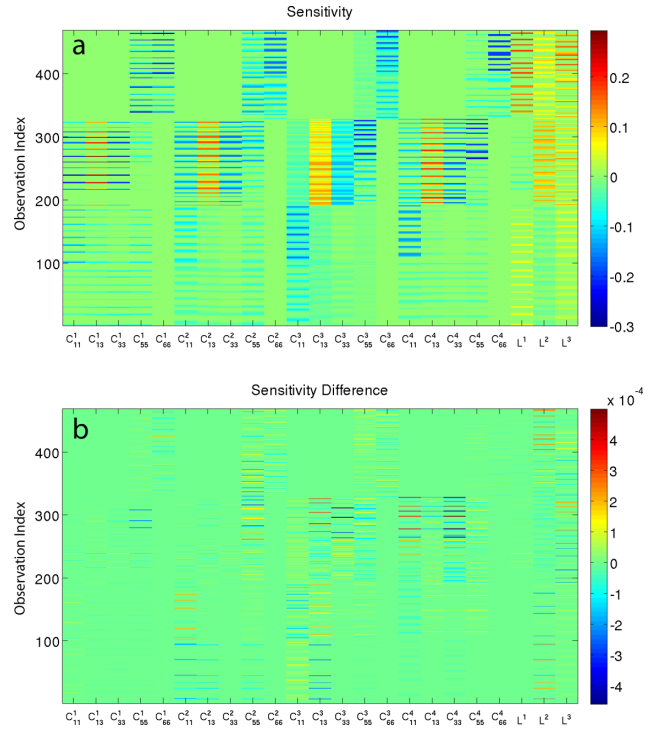

Figure 6. Analytical sensitivities (a) and their differences from the numerical ones (b) for the elastic moduli (C_{ij}^k) and layer thickness (L^k), with the superscript being the layer index. The rows correspond to different observations from different events to different receivers for qP, qSV and SH waves. Note the thickness of the fourth layer (L^4) is a null parameter in our inversion and thus is not shown.

analytical calculation of the sensitivity with respect to the elastic modulus, the ray path is assumed to be stationary (not changed with small perturbation). However, in the numerical calculation, there is no such assumption of stationarity.

Using the model shown in Fig. 5, we calculate and compare the analytical derivatives and numerical derivatives. In Fig. 6, approximately the first one third of the rows are the sensitivities related to the qP waves, the second one third are the sensitivities related to the qSV waves and the last one third are the sensitivities related to the SH waves. Fig. 6 shows that the differences between the analytical ones and the numerical ones are, in general, less than 0.5 per cent. This comparison validates our derivations.

Fig. 7 shows the comparison between the sensitivity matrix A (including A^t and A^φ) and the differential sensitivity matrix $Q \cdot A$. As the backazimuths have null sensitivity with respect to the propagation medium in the 1-D layered anisotropic model, the last 130 rows related to the backazimuth sensitivities shown in the box in Fig. 7(a) are all zeros. It can be found that the differential sensitivities $Q \cdot A$ with respect to the medium (C_{ij} and L) have been significantly reduced compared to those in A (boxed section), while the sensitivities with respect to the hypocentre and origin time have been mostly retained. This is mainly caused by the model parametrization (model represented as layers) and the limited space span of microseismic events. If the model is represented as smaller cells or grid nodes and microseismic events are more widely distributed, the differential model sensitivities will be more sensitive to the model parameters around the microseismic source region, as described in Zhang & Thurber (2006). For the example shown in Fig. 5, the extended double-difference method in eq. (19) is most sensitive to event locations and origin times rather than the propagation medium
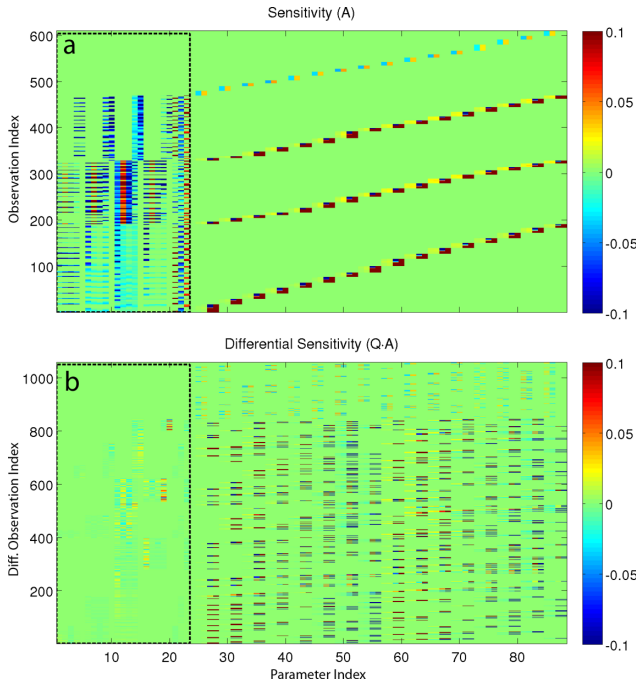
Figure 7. Comparison between the sensitivity matrix A (including A^t and A^φ) (a) and the differential sensitivity matrix $Q \cdot A$ (b). The rows correspond to the observations from different events to different receivers for qP, qSV and SH and backazimuths. The boxed section (23 columns) marks sensitivities or differential sensitivities with respect to the medium properties (C_{ij} and L), and the rest area indicates the sensitivities or differential sensitivities with respect to event hypocentres and origin times. Note Fig. 6(a) shows the same first 470 rows of the boxed section shown in Fig. 7(a) but in different colour scales for clarity. Here column normalization in A has been applied (Zhang & Thurber 2006) to balance different sensitivity magnitudes for different parameters, and thus comparison of the sensitivity magnitudes among different columns is not meaningful. A and $Q \cdot A$ are calculated for the final results given in Figs 10 and 12.

properties. This is the essential reason why the extended double-difference method is capable of providing better constraints in event relative locations. This also means the model parameters in this case are determined mostly with absolute traveltimes but not differential traveltimes.

After validating analytic model sensitivities, we first check the influence of seismic anisotropy on microseismic locations. Assuming only the velocities of the layers in the horizontal direction are acquired through perforation shots or string shots (Warpinski *et al.* 2009), but the model anisotropy parameters are unknown and thus the model is considered isotropic, we locate the events with both the traditional method (Fig. 8) and the extended double-difference method (differential method, Fig. 9), but with the velocity model fixed, using noise-free synthetic data. Note in this case the velocity inaccuracy does not affect the backazimuth. From Figs 8 and 9, it can be clearly seen that neither method gives correct absolute locations, as the velocity in the horizontal direction is faster than the velocity in any other direction for each layer. Therefore, the hypocentres are relocated further away from the correct locations. However, it also shows that the extended double-difference method incorporating differential arrival times and backazimuths improves relative locations of the events. The parallel factures in the two fracture systems can be depicted correctly from the double-difference location result while the traditional method gives distorted fractures. The ability to recover fracture geometry more correctly by
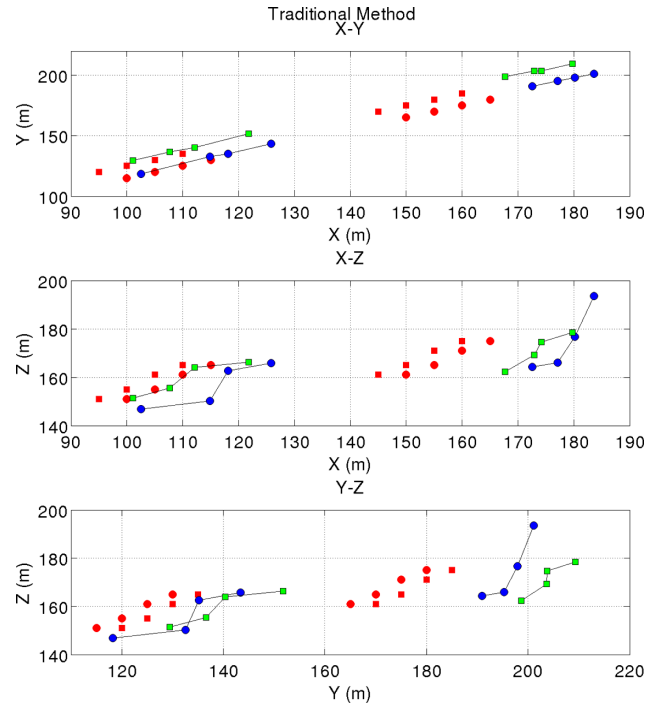

Figure 8. Relocated microseismic events in *X–Y*, *X–Z* and *Y–Z* planes using the absolute arrival times and backazimuths without inverting the anisotropy model parameters. Red dots and squares indicate the true event locations on the two fractures, respectively. Blue circles and green squares indicate the located events associated with the two fractures in each system, respectively.

the extended double-difference method lies in its advantage of removing some common model errors along ray paths caused by the inaccurate velocity model.

We now consider locating the events with simultaneous anisotropic tomography. To resemble realistic situations in our test, incoherent random noise for each traveltime observation ($\sigma = 0.2$ ms) and coherent random noise at each station (or random station term, $\sigma = 0.6$ ms) are added to the observed traveltimes. For the observed backazimuths, incoherent random noise for each backazimuth observation ($\sigma = 1°$) and coherent random noise at each station ($\sigma = 5°$) are added to the observed data. This is to simulate the fact that the coherent noise is generally greater than the random noise and the noise level added to the data is similar to that observed by Grechka *et al.* (2011) for data with reasonable quality. Fig. 10 shows the inverted elastic moduli and layer thicknesses starting with an isotropic model using the vertical *P*- and *S*-wave velocities and layer thicknesses that are different from the correct values by about 10 m. Due to different ray angle coverage, the elastic moduli are recovered with varying degrees of success for different layers in the presence of noise. The second and third layers with rays sampling at more different angles are recovered relatively well. At a given group angle, the sensitivity with respect to different elastic moduli varies, and thus the recovery accuracy for different elastic moduli also changes, given noisy observations from the limited number of hypocentres. The variation of sensitivity with respect to the group angle has been discussed in detail by Chapman & Miller (1996). In general, the tomography is ill conditioned when the rays only sample the medium in limited directions, especially when the source locations need to be determined simultaneously, as there is a trade-off between the velocity structure and the source locations (Zhang & Thurber 2006). Because there exist uncertainties for the inverted
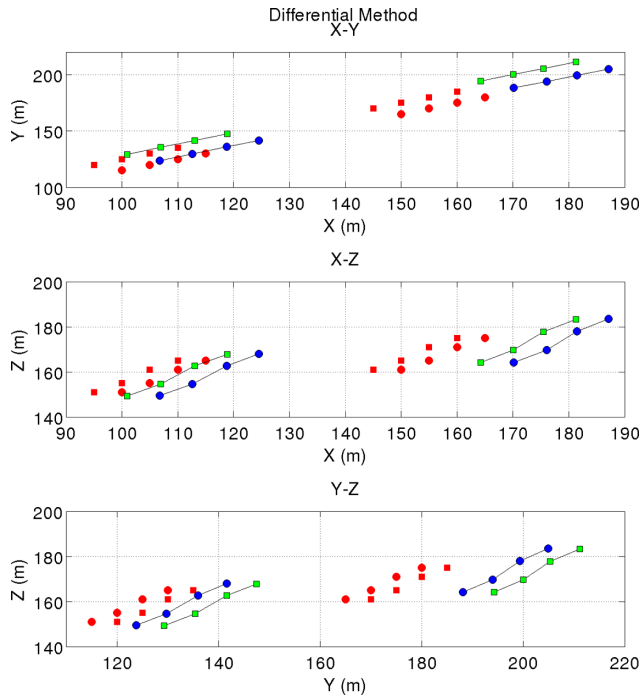
Figure 9. Same as Fig. 8 but for the extended double-difference method.
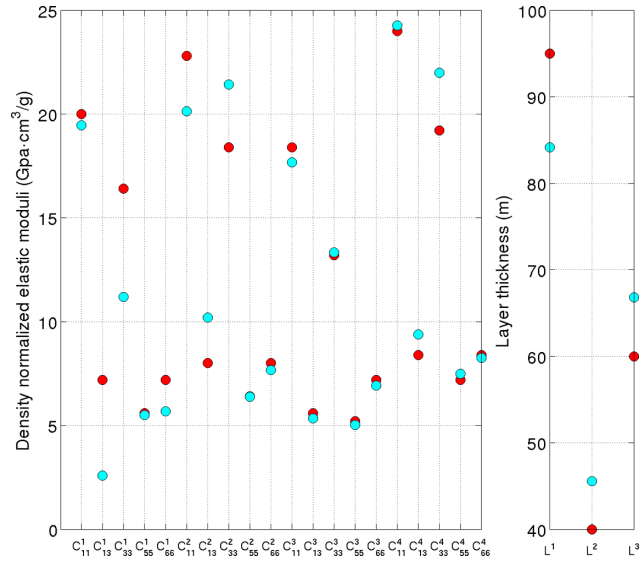

Figure 10. Comparison between true values of elastic moduli and layer thicknesses and inverted ones by the extended double-difference method. Red dots indicate the true parameter values and cyan dots indicate the inverted values.

Figure 11. Relocated microseismic events in *X–Y*, *X–Z* and *Y–Z* planes using the absolute arrival times and backazimuths with inverting anisotropy model parameters. Red dots and squares indicate the true event locations on the two fractures, respectively. Blue circles and green squares indicate the located events associated with the two fractures in each system, respectively.

Figure 12. Same as Fig. 11 but for the extended double-difference method.

elastic moduli for each layer, the thicknesses of the layers are also biased to some degree.

Figs 11 and 12 show the location results for both the traditional method, which only uses the absolute arrival times and backazimuths, and the extended double-difference method. Comparing the absolute locations, the two methods produce similar results. However, the relative locations of the events given by the extended double-difference method are much better than the traditional method, and the fractures are successfully delineated with clear parallelism recovered.

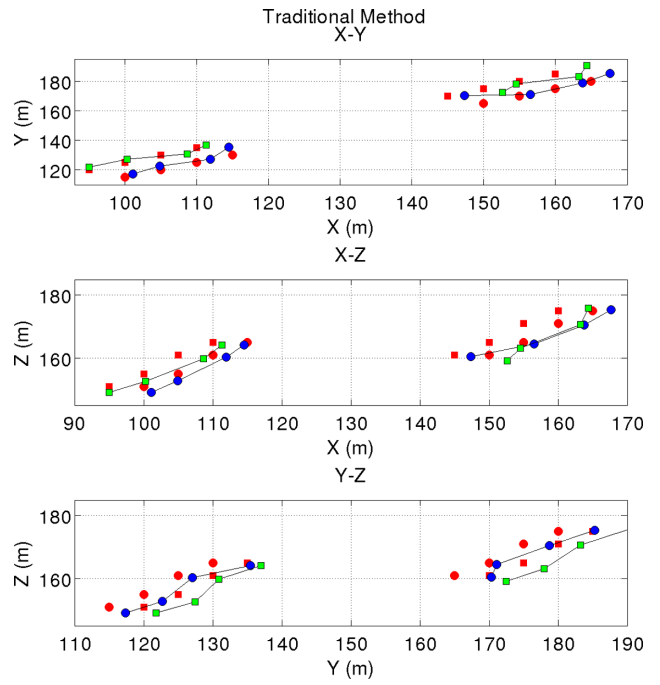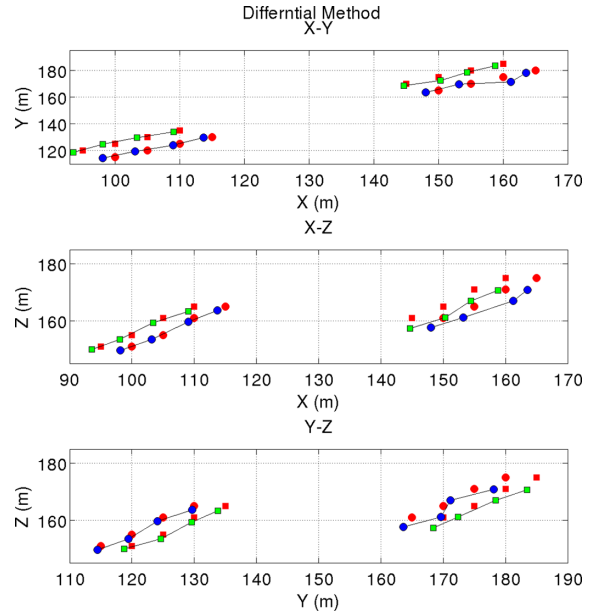In the second example, we use the anisotropic heterogeneous VTI model as shown in Fig. 2 to test our method in the presence of strong model heterogeneities. The event-receiver geometry together with the perturbed C_{11} model is shown in Fig. 13. In this test, three clusters of events associated with three fracture systems, each of which has eight events in two neighboring parallel fractures (four events on each fracture), are used as the passive sources for anisotropic tomography. The receivers are located at the same depth as in the first example, but the horizontal locations are shifted to (50, 50) m. All these events in the fractures are assumed to have the same source property, and a double-couple mechanism is used in our finite-difference code to generate the synthetic waveforms for all
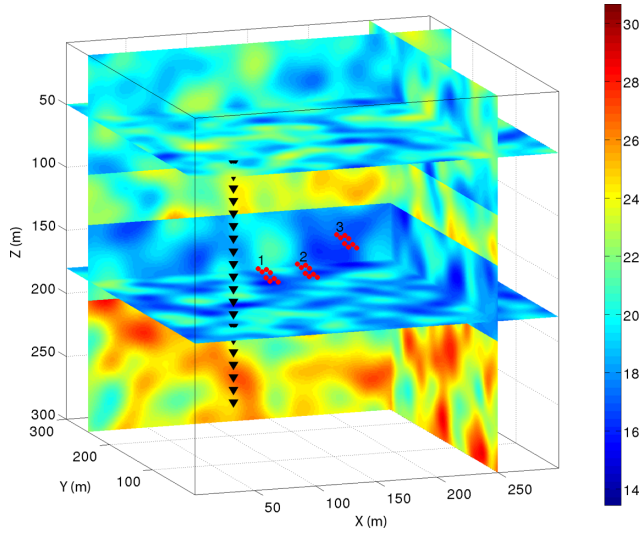
Figure 13. Randomly perturbed model for C_{11} (GPa cm^3 g^{-1}). This velocity model is the same as the one shown in Fig. 2, but there are three fracture systems.

events. Rodriguez *et al.* (2012) proposed a method to simultaneously invert for the source hypocentre and origin time, together with the source mechanism using a sparse representation theory.

In this case, we only use phase picks of qP, qSV and SH from randomly selected one third of the receivers for each event, and for different phases the random choice is different. The sparse observation resembles the situation where microseismic events are weak and the identifiable phases change with the receivers as the radiated energy of different types of waves varies with direction. The qP, qSV and SH traveltimes are manually picked from the synthetic seismograms generated by our in-house finite-difference wave propagation code. Note in this test we did not add any noise, because (1) we have already tested the influence of coherent and incoherent noises in the first example and (2) our manual phase picking can introduce some errors in the observed arrival times. Therefore, in this example the differences between the observed and modelled traveltimes consist of three origins: (1) the random perturbation on the elastic moduli, which cannot be captured in our tomography with layer VTI assumption, (2) picking errors and (3) errors introduced by high frequency ray approximation compared to finite frequency wave propagation. For this example we also start from an isotropic-layered velocity model as we do in the first one.

In this example, we obtained the differential arrival times by cross-correlating the waveforms, while obtaining the differential backazimuths by the method described in Appendix B. The absolute backazimuths are determined from the eigenvectors of the covariance matrix of the seismograms (Magotra *et al.* 1989). In Fig. 14, two events with a separation distance of 15 m in cluster 3 (the farthest cluster) are used as an example to show the similarity of waveforms after being shifted with the differential time given by waveform cross-correlation. The wiggles are aligned well after the shift, indicating correct differential arrival times have been determined. We found the differential backazimuths given by the method in Appendix B are similar to the differential backazimuths given by directly differentiating the absolute backazimuths at most receivers, as both approaches use waveform information automatically. In comparison, differential traveltimes obtained from waveform cross-correlation can often be more accurate than those from directly differentiating the manually picked absolute times
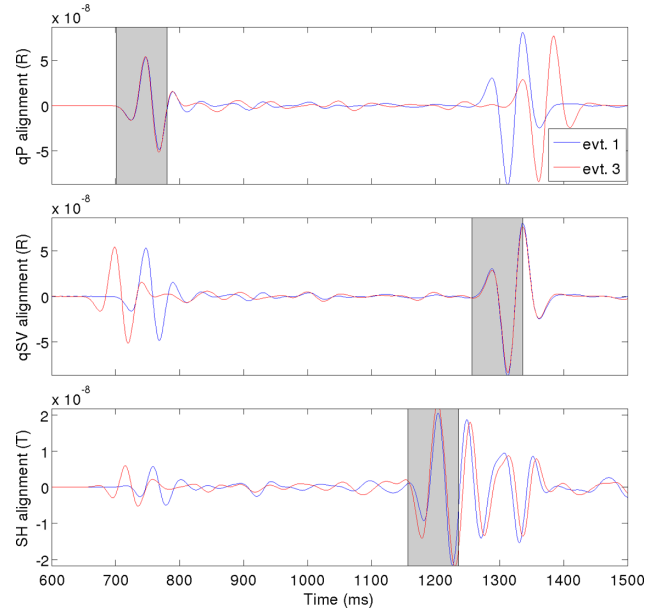

Figure 14. Waveform alignment for qP, qSV and SH phases for two events by waveform cross-correlation. The grey windows indicate the time window used for cross-correlation. The source wavelet used in the synthetic modelling is a Ricker wavelet with the central frequency $f_0 = 200$ Hz.
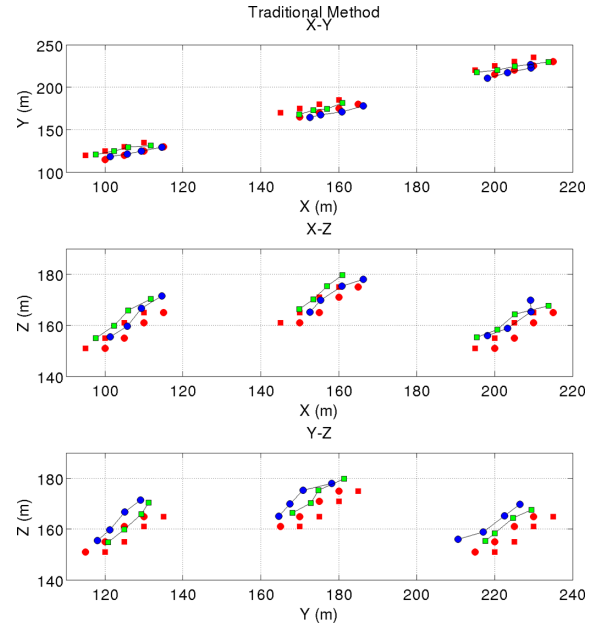

Figure 15. Relocated microseismic events in *X–Y*, *X–Z* and *Y–Z* planes for the second example using the absolute arrival times and backazimuths with inverting anisotropy model parameters. Red dots and squares indicate the true event locations on the two fractures, respectively. Blue circles and green squares indicate the located events associated with the two fractures in each system, respectively. There are three fracture systems in this example.

(Waldhauser & Ellsworth 2000). Note in our finite difference waveform modelling, we assume the events within one fracture system have the same mechanisms. This assumption should be reasonable considering the events occur at different segments of two parallel fractures and they are close in space.

Fig. 15 shows the event locations determined by the traditional method with joint anisotropic tomography. Due to the strong heterogeneity in the medium, the located events are shifted slightly away
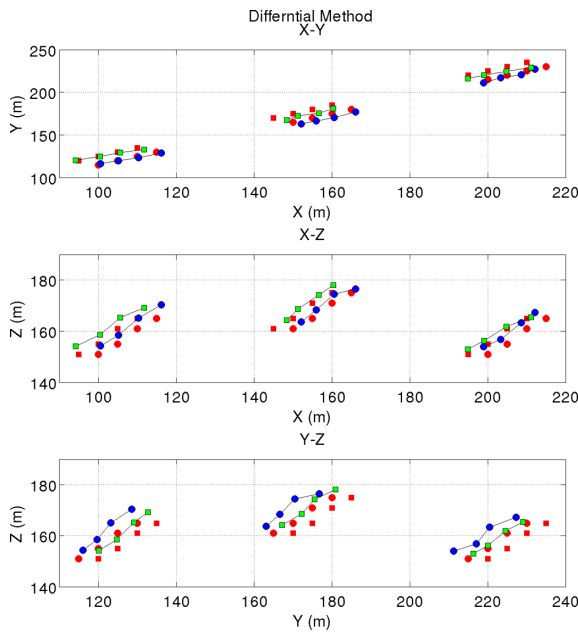
Figure 16. Same as Fig. 15 except for the extended double-difference method for the second example.

Figure 17. Comparison between true values of elastic moduli and layer thicknesses and inverted ones by the extended double-difference method. Red dots indicate the true parameter values and cyan dots indicate the inverted values. Note in the inversion the VTI layer model with constant elastic moduli for each layer is only an approximation for the randomly perturbed layer model used in generating the synthetic data.

from the true locations, especially in the vertical direction. As different phases (qP, qSV and SH) are included for location, the radial distances are in general constrained well (Eisner *et al.* 2009). Still, we found the relative locations of the events are poorly determined, for example, the events on one fracture can be mistakenly located onto the other fracture, and the spacing between some events is also resolved with considerable errors.

Fig. 16 shows the location result with the extended double-difference method with joint anisotropic tomography. Comparing Fig. 16 with Fig. 15, it can be found that the relative locations of the events have been improved considerably. For instance, in the *X–Y* plot (map view) where the relative locations are sensitive to both backazimuths and traveltimes, we find including the differential backazimuth information can improve the relative location substantially, yielding satisfactory delineation of the parallelism of the fractures and recovery of the spacing between events. It should be noted that the events in different clusters are located with varying accuracy, as the random heterogeneities have diverse influences on the traveltimes and backazimuth of events at different locations. The side views also show improvement in relative location with the extended double-difference method.

Fig. 17 shows the anisotropic tomography result. Note in the inversion the VTI layer model with constant elastic moduli for each layer is only an approximation for the randomly perturbed layer model used in generating the synthetic waveform data. Similar to the previous example, elastic moduli in different layers and the layer thicknesses are recovered with varying degrees of closeness to the reference values.

4 CONCLUSIONS

In this research, we extend the double-difference location method to use both differential arrival times and differential backazimuths to locate the microseismic events. We also develop an anisotropic tomography method to determine elastic modulus and layer thickness of the VTI medium using the arrival times of microseismic events. The extended double-difference location system is combined together with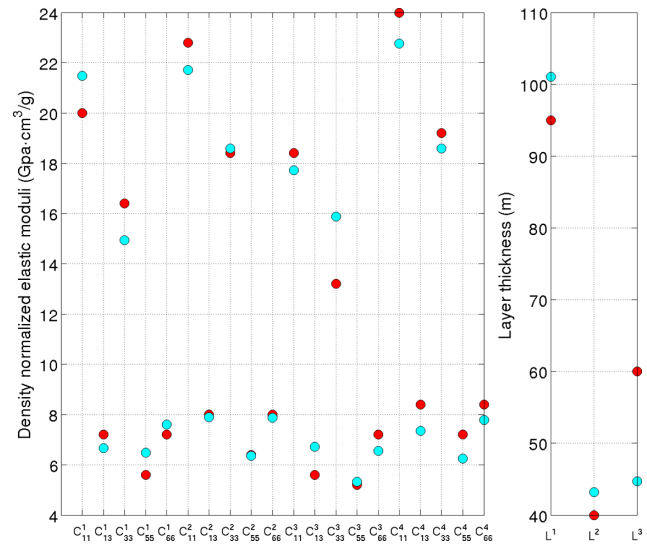 the anisotropy tomography system to simultaneously locate microseismic events and determine model parameters. The location improvement from tomography and from double-difference constraints is complimentary, as the former one improves the absolute locations and the latter one improves the relative locations. The additional differential backazimuth information is extracted from available seismic records and thus this method does not require collecting any new data. We derived analytical sensitivities for elastic modulus and layer thickness for anisotropy tomography without any weak anisotropy assumption. We also compared our analytical sensitivities with numerical sensitivities to validate our derivations. With inaccuracy in traveltimes and backazimuths either from noise or from model heterogeneities, the velocity structure (elastic moduli and layer thicknesses) can be recovered with varying degrees of success, depending on the ray coverage. It is shown that mostly the absolute traveltimes, but not the differential traveltimes, help to improve the velocity model due to the layer parametrization. From synthetic tests, it is shown absolute event locations are significantly biased without considering anisotropy for the layered VTI model. Synthetic examples show that our new method with the differential information can produce better relative locations of the microseismic events and, therefore, delineate the fractures more clearly and resolve the spacing between events with better accuracy. Both characteristics are important in hydraulic fracturing monitoring, as the former one is critical for understanding the striking of fractures, while the latter one is critical for understanding pressure propagation from the injection well. The pure analytical calculations involved in our inversion scheme make this method fast and accurate, and thus it is especially suitable for real time monitoring of the shale gas/oil production.

REFERENCES

Bulant, P., Eisner, L., Pšenčík, I. & Le Calvez, J., 2007. Importance of borehole deviation surveys for monitoring of hydraulic fracturing treatments, *Geophys. Prospect.,* **55,** 891–899.

Castellanos, F. & van der Baan, M., 2012. High-accuracy relative event locations using a combined multiplet analysis and the double-difference inversion, in *Proceedings of the Annual Meeting Society of Exploration Geophysists, Extended Abstract, Las Vegas,* doi:10.1190/segam2012-0829.1.

Chapman, C.H. & Miller, D.E., 1996. Velocity sensitivity in transversely isotropic media, *Geophys. Prospect.,* **44,** 525–549.

De Meersman, K., Kendall, J.M. & van der Baan, M., 2009. The 1998 Valhall microseismic data set: an integrated study of relocated sources, seismic multiplets, and S-wave splitting, *Geophysics,* **74,** B183–B195.

Eisner, L. *et al.*, 2009. Uncertainties in passive seismic monitoring, *Leading Edge,* **28,** 648–655.

Eisner, L. *et al.*, 2010. Comparison of surface and borehole locations of induced seismicity, *Geophys. Prospect.,* **58,** 809–820.

Foulger, G.R. & Julian, B.R., 2011. Earthquake and errors: methods for industrial applications, *Geophysics,* **76,** WC5–WC15.

Grechka, V., Singh, P. & Das, I., 2011. Estimation of effective anisotropy simultaneously with locations of microseismic events, *Geophysics,* **76,** WC141–WC153.

Levenberg, K., 1944. A method for the solution of certain non-linear problems in least squares, *Quart. Appl. Math.,* **2,** 164–168.

Li, J.L. *et al.*, 2011. Focal mechanism determination of induced microearthquakes in an oil field using full waveforms from shallow and deep seismic networks, *Geophysics,* **76,** WC87–WC101.

Magotra, N., Ahmed, N. & Chael, E., 1989. Single-station seismic event detection and location, *IEEE Trans. Geosci. Remote Sens.,* **27,** 15–23.

Mah, M. & Schmitt, D.R., 2003. Determination of the complete elastic stiffnesses from ultrasonic phase velocity measurements, *J. geophys. Res.,* **108**(B1), 2016.

Maxwell, S.C., 2010. Microseismic: growth born from success, *Leading Edge,* **29,** 338–343.

Maxwell, S.C. *et al.*, 2010. Petroleum reservoir characterization using downhole microseismic monitoring, *Geophysics,* **75,** A129–A137.

Moczo, P., Robertsson, J.O.A. & Eisner, L., 2007. *Adv. Geophys.,* **48,** 421–508.

Nihei, K.T. *et al.*, 2011. Phased array compaction cell for measurement of the transversely isotropic elastic properties of compacting sediments, *Geophysics,* **76**(3), WA113–WA123.

Rodriguez, I.V., Sacchi, M. & Gu, Y.J., 2012. Simultaneous recovery of origin time, hypocentre location and seismic moment tensor using sparse representation theory, *Geophys. J. Int.,* **188,** 1188–1202.

Rutledge, J.T. & Phillips, W.S., 2003. Hydraulic stimulation of natural fractures as revealed by induced microearthquakes, Carthage Cotton Valley gas field, east Texas, *Geophysics,* **68,** 441–452.

Rutledge, J.T., Phillips, W.S. & Schuessler, B.K., 1998. Reservoir characterization using oil-production-induced microseismicity, Clinton County, Kentucky, *Tectonophysics,* **289,** 129–152.

Song, F.X. *et al.*, 2010. An improved method for hydrofracture-induced microseismic event detection and phase picking, *Geophysics,* **75,** A47–A52.

Tang, W. & Li, L., 2008. Exact traveltime computation in multi-layered transversely isotropic media with vertical symmetry axis, *Acta Seismol. Sin.,* **21,** 370–379.

Thomsen, L., 1986. Weak elastic anisotropy, *Geophysics,* **51,** 1954–1966.

Van Dok, R. *et al.*, 2011. Seismic anisotropy in microseismic event location analysis, *Leading Edge,* **30,** 766–770.

Waldhauser, F. & Ellsworth, W.L., 2000. A double-difference earthquake location algorithm: method and application to the northern Hayward fault, California, *Bull. seism. Soc. Am.,* **90,** 1353–1368.

Warpinski, N.R. *et al.*, 2005. Improved microseismic fracture mapping using perforation timing measurements for velocity calibration, in *Proceedings of the SPE Annual Technical Conference and Exhibition*, 2003 October 5–8, Denver, Colorado, Paper 84488.

Warpinski, N.R. *et al.*, 2009. Anisotropy effects in microseismic monitoring, in *Proceedings of the SPE Annual Technical Conference and Exhibition,* 2009 October 4–7, New Orleans, LA, paper 124208.

Wolfe, C.J., 2002. On the mathematics of using difference operators to relocate earthquakes, *Bull. seism. Soc. Am.,* **92,** 2879–2892.

Zhang, H.J. & Thurber, C.H., 2003. Double-difference tomography: the method and its application to the Hayward Fault, California, *Bull. seism. Soc. Am.,* **93,** 1875–1889.

Zhang, H.J. & Thurber, C.H., 2006. Development and applications of double-difference seismic tomography, *Pure appl. Geophys.,* **163,** 373–403.

Zhang, H.J. *et al.*, 2009. Passive seismic tomography using induced seismicity at a petroleum field in Oman, *Geophysics,* **74,** WCB57–WCB69.

Zhang, J. & Toksoz, M.N., 1998. Nonlinear refraction travel time tomography, *Geophysics,* **63,** 1726–1737.

Zhou, B. & Greenhalgh, S.A., 2005. Analytic expressions for the velocity sensitivity to the elastic moduli for the most general anisotropic media, *Geophys. Prospect.,* **53,** 619–641.

Zimmer, 2011. Microseismic design studies, *Geophysics,* **76,** WC17–WC25.

APPENDIX A: APPROXIMATION OF THE BACKAZIMUTH SENSITIVITY

In any heterogeneous anisotropic medium, the derivatives in eq. (8) can be approximated with the following finite difference schemes. For the first derivatives at the receiver location, they are the phase slowness, and can be approximated using second order finite-difference, for example:

$$\frac{\partial T}{\partial x_r} \approx \frac{T\left(x_r + \Delta x, y_r, z_r; x_s, y_s, z_s\right) - T\left(x_r - \Delta x, y_r, z_r; x_s, y_s, z_s\right)}{2\Delta x}. \tag{A1}$$

For the second derivatives, they can be approximated, for example, as:

$$\frac{\partial \left(\frac{\partial T}{\partial x_r}\right)}{\partial x_s} \approx \frac{T\left(x_r + \Delta x, y_r, z_r; x_s + \Delta x, y_s, z_s\right) - T\left(x_r + \Delta x, y_r, z_r; x_s - \Delta x, y_s, z_s\right)}{4\Delta x^2}$$
$$- \frac{T\left(x_r - \Delta x, y_r, z_r; x_s + \Delta x, y_s, z_s\right) - T\left(x_r - \Delta x, y_r, z_r; x_s - \Delta x, y_s, z_s\right)}{4\Delta x^2}. \tag{A2}$$

The other second derivatives can also be calculated numerically by adding the finite increment $\pm\Delta l$ to different coordinate variables.

APPENDIX B: CALCULATION OF THE DIFFERENTIAL BACKAZIMUTH

Here we describe a method that can determine the differential backazimuth ($\Delta\varphi$) from the observed waveforms without the need to solve the eigenvalue problems. Let us denote the signals from the first event as $p_1(t_n)$ and the signals from the second event as $p_2(t_n)$, which are column vectors. Then the observed seismograms in the north and east components are:

$$n_1(t_n) = p_1(t_n)\sin(\varphi_1)$$
$$e_1(t_n) = p_1(t_n)\cos(\varphi_1)$$

(B1)

and

$$n_2(t_n) = p_2(t_n)\sin(\varphi_2)$$
$$e_2(t_n) = p_2(t_n)\cos(\varphi_2)$$

(B2)

for the first and second events, respectively. Here φ_1 and φ_2 are the averaged backazimuths of the signals in the observation windows.

Then

$$n_1^T n_2 + e_1^T e_2 = p_1^T p_2 \sin(\varphi_1)\sin(\varphi_2) + p_1^T p_2 \cos(\varphi_1)\cos(\varphi_2) = p_1^T p_2 \cos(\varphi_1 - \varphi_2)$$
$$n_1^T e_2 - e_1^T n_2 = p_1^T p_2 \sin(\varphi_1)\cos(\varphi_2) - p_1^T p_2 \cos(\varphi_1)\sin(\varphi_2) = p_1^T p_2 \sin(\varphi_1 - \varphi_2).$$

(B3)

The differential backazimuth angle can be given by

$$\tan(\Delta\varphi) = \tan(\varphi_1 - \varphi_2) = \frac{p_1^T p_2 \sin(\varphi_1 - \varphi_2)}{p_1^T p_2 \cos(\varphi_1 - \varphi_2)} = \frac{n_1^T e_2 - e_1^T n_2}{n_1^T n_2 + e_1^T e_2}.$$

(B4)

The derivations above do not assume any similarity between signals $p_1(t_n)$ and $p_2(t_n)$, that is, they can be of different frequencies and amplitudes and eq. (B4) is still valid. Nevertheless, windowing around the first arrivals of the seismograms is needed, otherwise the determined $\Delta\varphi$ does not reflect the differential backazimuth in the first arrivals but rather is an averaged result. Also, eq. (B4) does not require $p_1(t_n)$ and $p_2(t_n)$ to be synchronized in theory. But we found the determined differential backazimuths are most accurate when two traces are first aligned by waveform cross-correlation (performed when determining the differential traveltimes), as $p_1^T p_2$ is maximized and has the best signal-to-noise ratio when two signals are in phase.

APPENDIX C: DERIVATION OF THE SENSITIVITIES WITH RESPECT TO C_{ij}

To calculate the traveltime along the ray path, we need to calculate the group velocity associated with the ray. For qP, qSV or SH, the group velocity v_g and the phase velocity v are related by

$$v_g^2[\Phi(\theta)] = v^2(\theta) + \left(\frac{dv}{d\theta}\right)^2 = v^2(\theta) + \frac{1}{4v^2}\left(\frac{dv^2}{d\theta}\right)^2,$$

(C1)

where the group angle $\Phi(\theta)$ and the phase angle θ differ by $\Delta\theta$:

$$\Phi(\theta) - \theta = \Delta\theta$$

(C2)

and $\Delta\theta$ can be found by

$$\tan(\Delta\theta) = \frac{1}{v}\frac{dv}{d\theta} = \frac{1}{2v^2}\frac{dv^2}{d\theta}.$$

(C3)

The derivative of the phase velocity with respect to the phase angle is given by

$$\frac{\partial v_{P,SV}^2}{\partial\theta} = \frac{1}{2}\frac{\partial[C_{33} + C_{55} + (C_{11} - C_{33})\sin^2(\theta) \pm D(\theta)]}{\partial\theta} = (C_{11} - C_{33})\sin(\theta)\cos(\theta) \pm \frac{1}{4}\left[\frac{D_1 \sin(2\theta) + 4D_2 \sin^3(\theta)\cos(\theta)}{D(\theta)}\right],$$

(C4)

where

$$D_1 = 2\left[2(C_{13} + C_{55})^2 - (C_{33} - C_{55})(C_{11} + C_{33} - 2C_{55})\right]$$

$$D_2 = (C_{11} + C_{13} - 2C_{55})^2 - 4(C_{13} + C_{55})^2$$

$$D = \left[(C_{33} - C_{55})^2 + D_1 \sin^2(\theta) + D_2 \sin^4(\theta)\right]^{\frac{1}{2}}.$$

(C5)

And for SH wave

$$\frac{\partial v_{SH}^2}{\partial\theta} = C_{66}\sin(2\theta) - C_{55}\sin(2\theta)$$

(C6)

C.1 qP, qSV

The sensitivity of the phase velocity for qP and qSV waves with respect to the density-normalized elastic modulus C_{ij} is:

$$\frac{\partial v_{P,SV}^2}{\partial C_{ij}} = \frac{1}{2}\left[\frac{\partial (C_{33}+C_{55})}{\partial C_{ij}} + \frac{\partial (C_{11}-C_{33})}{\partial C_{ij}}\sin^2(\theta) + (C_{11}-C_{33})\sin(2\theta)\frac{\partial \theta}{\partial C_{ij}} \pm \frac{\partial D(\theta)}{\partial C_{ij}}\right], \tag{C7}$$

where the plus sign is for qP wave, and the minus sign is for qSV wave. There are two derivatives we need to find, namely $\partial\theta/\partial C_{ij}$ and $\partial D(\theta)/\partial C_{ij}$. For the first term $\partial\theta/\partial C_{ij}$,

$$\frac{\partial \theta}{\partial C_{ij}} = \frac{\partial \left(\theta_g - \Delta\theta\right)}{\partial C_{ij}} = -\frac{\partial \Delta\theta}{\partial C_{ij}} = -\frac{\partial \mathrm{atan}\left(\frac{1}{2v^2}\frac{\partial v^2}{\partial \theta}\right)}{\partial C_{ij}} = \frac{-1}{1+\left(\frac{1}{2v^2}\frac{\partial v^2}{\partial \theta}\right)^2}\frac{\partial \left(\frac{1}{2v^2}\frac{\partial v^2}{\partial \theta}\right)}{\partial C_{ij}}. \tag{C8}$$

Here comes the only assumption in our derivation: $\partial\theta_g/\partial C_{ij} = 0$. The ray stationarity is valid as the ray path (group angle) perturbation is of higher order to the traveltime perturbation, and is often used in isotropic traveltime tomography (Zhang & Toksoz 1998).

Define $A_d = 1/[1+(\frac{1}{2v^2}\frac{\partial v^2}{\partial \theta})^2]$, $\partial\theta/\partial C_{ij}$ can be further simplified as:

$$\frac{\partial \theta}{\partial C_{ij}} = -A_d\frac{\partial \left(\frac{1}{2v^2}\frac{\partial v^2}{\partial \theta}\right)}{\partial C_{ij}} = -A_d\left[-\frac{1}{2v^4}\frac{\partial v^2}{\partial \theta}\frac{\partial v^2}{\partial C_{ij}} + \frac{1}{2v^2}\frac{\partial \left(\frac{\partial v^2}{\partial \theta}\right)}{\partial C_{ij}}\right]. \tag{C9}$$

Eq. (C9) is a general expression for qP, qSV and SH waves. The term $\partial(\frac{\partial v^2}{\partial\theta})/\partial C_{ij}$ for qP and qSV waves can be derived from eq. (C4):

$$\frac{\partial \left(\frac{\partial v^2}{\partial \theta}\right)}{\partial C_{ij}} = \frac{\partial (C_{11}-C_{33})}{\partial C_{ij}}\sin(\theta)\cos(\theta) + (C_{11}-C_{33})\cos(2\theta)\frac{\partial \theta}{\partial C_{ij}}$$

$$\pm\frac{1}{4}\left[\frac{1}{D(\theta)}\left(\frac{\partial D_1}{\partial C_{ij}}\sin(2\theta) + 2D_1\cos(2\theta)\frac{\partial \theta}{\partial C_{ij}} + 4\frac{\partial D_2}{\partial C_{ij}}\sin^3(\theta)\cos(\theta) + 4D_2\left(3\sin^2(\theta)\cos^2(\theta)-\sin^4(\theta)\right)\frac{\partial \theta}{\partial C_{ij}}\right)\right.$$

$$\left. + \left(D_1\sin(2\theta) + 4D_2\sin^3(\theta)\cos(\theta)\right)\left(-\frac{1}{D^2(\theta)}\right)\frac{\partial D(\theta)}{\partial C_{ij}}\right] \tag{C10}$$

where

$$\frac{\partial D_1}{\partial C_{ij}} = 2\left[4(C_{13}+C_{55})\frac{\partial (C_{13}+C_{55})}{\partial C_{ij}} - \frac{\partial (C_{33}-C_{55})}{\partial C_{ij}}(C_{11}+C_{33}-2C_{55}) - (C_{33}-C_{55})\frac{\partial (C_{11}+C_{33}-2C_{55})}{\partial C_{ij}}\right]$$

$$\frac{\partial D_2}{\partial C_{ij}} = 2(C_{11}+C_{33}-2C_{55})\frac{\partial (C_{11}+C_{33}-2C_{55})}{\partial C_{ij}} - 8(C_{13}+C_{55})\frac{\partial (C_{13}+C_{55})}{\partial C_{ij}}. \tag{C11}$$

And the derivative $\partial D(\theta)/\partial C_{ij}$ is given by

$$\frac{\partial D(\theta)}{\partial C_{ij}} = \frac{1}{2D(\theta)}\left(2(C_{33}-C_{55})\frac{\partial (C_{33}-C_{55})}{\partial C_{ij}} + \frac{\partial D_1}{\partial C_{ij}}\sin^2(\theta) + D_1\sin(2\theta)\frac{\partial \theta}{\partial C_{ij}} + \frac{\partial D_2}{\partial C_{ij}}\sin^4(\theta) + 4D_2\sin^3(\theta)\cos(\theta)\frac{\partial \theta}{\partial C_{ij}}\right). \tag{C12}$$

Substituting eqs (C7), (C10), (C11) and (C12) into eq. (C9), we obtain an equation containing only one unknown term $\partial\theta/\partial C_{ij}$. Combine the terms and solve for $\partial\theta/\partial C_{ij}$:

$$
\left\{1 - \frac{A_d}{4v^4}\frac{\partial v^2}{\partial\theta}\left[(C_{11}-C_{33})\sin(2\theta) \pm \frac{1}{2D(\theta)}\left(D_1\sin(2\theta) + \frac{\partial D_2}{\partial C_{ij}}\sin^4(\theta) + 4D_2\sin^3(\theta)\cos(\theta)\right)\right]\right.
$$

$$
+ \frac{A_d}{2v^2}\left[(C_{11}-C_{33})\cos(2\theta) \pm \frac{1}{4}\frac{1}{D(\theta)}(2D_1\cos(2\theta) + 4D_2(3\sin^2(\theta)\cos^2(\theta) - \sin^4(\theta)))\right.
$$

$$
\left.\left.\pm\frac{1}{4}(D_1\sin(2\theta) + 4D_2\sin^3(\theta)\cos(\theta))\left(-\frac{1}{2D^3(\theta)}\right)(D_1\sin(2\theta) + 4D_2\sin^3(\theta)\cos(\theta))\right]\right\}\frac{\partial\theta}{\partial C_{ij}}
$$

$$
= \frac{A_d}{4v^4}\frac{\partial v^2}{\partial\theta}\left[\frac{\partial(C_{33}+C_{55})}{\partial C_{ij}} + \frac{\partial(C_{11}-C_{33})}{\partial C_{ij}}\sin^2(\theta)\right.
$$

$$
\left.\pm\frac{1}{2D(\theta)}\left(2(C_{33}-C_{55})\frac{\partial(C_{33}-C_{55})}{\partial C_{ij}} + \frac{\partial D_1}{\partial C_{ij}}\sin^2(\theta) + \frac{\partial D_2}{\partial C_{ij}}\sin^4(\theta)\right)\right]
$$

$$
- \frac{A_d}{2v^2}\left[\frac{\partial(C_{11}-C_{33})}{\partial C_{ij}}\sin(\theta)\cos(\theta) \pm \frac{1}{4D(\theta)}\left(\frac{\partial D_1}{\partial C_{ij}}\sin(2\theta) + 4\frac{\partial D_2}{\partial C_{ij}}\sin^3(\theta)\cos(\theta)\right)\right.
$$

$$
\left.\pm\frac{1}{4}(D_1\sin(2\theta) + 4D_2\sin^3(\theta)\cos(\theta))\left(-\frac{1}{2D^3(\theta)}\right)\left(2(C_{33}-C_{55})\frac{\partial(C_{33}-C_{55})}{\partial C_{ij}} + \frac{\partial D_1}{\partial C_{ij}}\sin^2(\theta) + \frac{\partial D_2}{\partial C_{ij}}\sin^4(\theta)\right)\right]. \quad (C13)
$$

After solving for $\partial\theta/\partial C_{ij}$, we can then solve for $\partial D(\theta)/\partial C_{ij}$ with eq. (C12); then with $\partial\theta/\partial C_{ij}$ and $\partial D(\theta)/\partial C_{ij}$, we can solve for $\partial v^2/\partial C_{ij}$ with eq. (C7) and for $\partial(\frac{\partial v^2}{\partial\theta})/\partial C_{ij}$ with eq. (C10), respectively. With the latter two terms, we can finally obtain $\partial v_g/\partial C_{ij}$ with eq. (15).

C.2 SH wave

The derivation of the SH sensitivity is similar to that of qP and qSV, and we can follow a similar but simpler procedure. For SH wave,

$$
\frac{\partial v^2}{\partial C_{ij}} = \frac{\partial\left(C_{55} + (C_{66}-C_{55})\sin^2(\theta)\right)}{\partial C_{ij}}
$$

$$
\frac{\partial\left(\frac{\partial v^2}{\partial\theta}\right)}{\partial C_{ij}} = \frac{\partial\left((C_{66}-C_{55})\sin(2\theta)\right)}{C_{ij}}. \quad (C14)
$$

Substituting eq. (C14) into eq. (15) for the sensitivity of group velocity:

$$
\frac{\partial v_g}{dC_{ij}} = \frac{1}{2v_g}\left[\frac{\partial\left(C_{55}+(C_{66}-C_{55})\sin^2(\theta)\right)}{\partial C_{ij}}\left(1 - \frac{1}{4v^4}\left(\frac{\partial v^2}{\partial\theta}\right)^2\right) + \frac{1}{2v^2}\frac{\partial v^2}{\partial\theta}\frac{\partial\left((C_{66}-C_{55})\sin(2\theta)\right)}{C_{ij}}\right]. \quad (C15)
$$

And then into eq. (C9) for the sensitivity of phase angle:

$$
\frac{\partial\theta}{\partial C_{ij}} = A_d\left[\frac{1}{2v^4}\frac{\partial v^2}{\partial\theta}\left(\frac{\partial\left(C_{55}+(C_{66}-C_{55})\sin^2(\theta)\right)}{\partial C_{ij}}\right) - \frac{1}{2v^2}\frac{\partial\left((C_{66}-C_{55})\sin(2\theta)\right)}{C_{ij}}\right]. \quad (C16)
$$

For SH wave, we can write explicitly for $\partial\theta/\partial C_{55}$ and $\partial\theta/\partial C_{66}$:

$$
\left[1 - A_d\frac{1}{2v^4}\frac{\partial v^2}{\partial\theta}(C_{66}-C_{55})\sin(2\theta) + \frac{A_d}{v^2}(C_{66}-C_{55})\cos(2\theta)\right]\frac{\partial\theta}{\partial C_{55}} = A_d\left[\frac{1}{2v^4}\frac{\partial v^2}{\partial\theta}\cos^2(\theta) + \frac{1}{v^2}\sin(\theta)\cos(\theta)\right]
$$

$$
\left[1 - A_d\frac{1}{2v^4}\frac{\partial v^2}{\partial\theta}(C_{66}-C_{55})\sin(2\theta) + \frac{A_d}{v^2}(C_{66}-C_{55})\cos(2\theta)\right]\frac{\partial\theta}{\partial C_{66}} = A_d\left[\frac{1}{2v^4}\frac{\partial v^2}{\partial\theta}\sin^2(\theta) - \frac{1}{v^2}\sin(\theta)\cos(\theta)\right]. \quad (C17)
$$

Then following a similar procedure as for qP and qSV waves, we can solve for the sensitivity of SH waves with respect to the elastic moduli.

APPENDIX D: CONSTRAINT OPERATOR P^c

In some cases, shale gas/oil drilling companies can make core samples of the subsurface structure and determined some of the Thomsen's anisotropy parameters by measuring wave velocities at different directions. In our inversion, each C_{ij} is inverted independently, but their certain

combinations, which give the Thomsen's anisotropy parameters, should be kept close to the values determined by the lab measurements. Therefore, we propose the following linear operators to constrain such combinations in eq. (19):

$$\frac{C_{11} - C_{33}}{2C_{33}} = \varepsilon \rightarrow C_{11} - (2\varepsilon + 1)C_{33} = 0 \tag{D1}$$

$$\frac{C_{13} + 2C_{55} - C_{33}}{C_{33}} \approx \delta \rightarrow C_{13} + 2C_{55} - (\delta + 1)C_{33} = 0 \tag{D2}$$

$$\frac{C_{66} - C_{55}}{2C_{55}} = \gamma \rightarrow C_{66} - (2\gamma + 1)C_{55} = 0. \tag{D3}$$

Note the expression for δ is approximate here as a linear relation between the elastic moduli C_{ij} and the anisotropic parameters is required. The anisotropy parameters ε, δ and γ here are constants determined by lab measurements, if available. These additional constraints can also help to reduce the ill condition and resulting non-uniqueness in the inversion for anisotropy.